Non-proteinaceous hydrolase comprised of a phenylalanine metallo-supramolecular amyloid-like structure

Pandeeswar Makam[1], Sharma S. R. K. C. Yamijala[2], Kai Tao [1], Linda J. W. Shimon [3], David S. Eisenberg[4], Michael R. Sawaya[4], Bryan M. Wong [2,5] and Ehud Gazit [1,6]*

[1]Department of Molecular Microbiology and Biotechnology, George S. Wise Faculty of Life Sciences, Tel Aviv University, Tel Aviv, Israel. [2]Department of Chemical and Environmental Engineering, University of California, Riverside, CA, USA. [3]Chemical Research Support, The Weizmann Institute of Science, Rehovot, Israel. [4]Department of Biological Chemistry and Department of Chemistry and Biochemistry, Howard Hughes Medical Institute, UCLA–DOE Institute for Genomics and Proteomics, University of California Los Angeles, Los Angeles, CA, USA. [5]Department of Physics and Astronomy, and Materials Science and Engineering Program, University of California, Riverside, CA, USA. [6]Department of Materials Science and Engineering, Iby and Aladar Fleischman Faculty of Engineering, Tel Aviv University, Tel Aviv, Israel. *e-mail: ehudg@post.tau.ac.il

Supplementary Information

Nonproteinaceous hydrolase comprised of phenylalanine metallo-supramolecular amyloid-like structure

Pandeeswar Makam[1], Sharma S. R. K. C. Yamijala[2], Kai Tao[1], Linda J.W. Shimon[3], David S. Eisenberg[4], Michael R. Sawaya[4], Bryan M. Wong[2,5], Ehud Gazit[1,6]*

Affiliations:

[1]Department of Molecular Microbiology and Biotechnology, George S. Wise Faculty of Life Sciences, Tel Aviv University, Tel Aviv 6997801, Israel.

[2]Department of Chemical & Environmental Engineering, University of California, Riverside, CA, 92521, USA.

[3]Chemical Research Support, The Weizmann Institute of Science, 7610001 Rehovot, Israel

[4]Department of Biological Chemistry and Department of Chemistry and Biochemistry, University of California Los Angeles (UCLA), Howard Hughes Medical Institute (HHMI), UCLA–Department of Energy (DOE) Institute for Genomics and Proteomics, Los Angeles, CA 90095, USA.

[5]Department of Physics & Astronomy, and Materials Science & Engineering Program, University of California, Riverside, CA, 92521, USA.

[6]Department of Materials Science and Engineering, Iby and Aladar Fleischman Faculty of Engineering, Tel Aviv University, Tel Aviv 6997801, Israel.

*Correspondence to: Ehud Gazit. (ehudg@post.tau.ac.il).

Supplementary methods

Materials

L-phenylalanine (F), zinc chloride (ZnCl$_2$), p-nitrophenyl acetate (pNPA), p-nitrophenol (pNP), p-nitrophenyl phosphate (pNPP), p-nitrophenyl β–D-glucopyranoside (pNPG), O,O-dimethyl O-(4-nitrophenyl) phosphate (pNPP), N-methyl-2-pyrrolidone (NMP), phenol red and sodium hydroxide (NaOH) were purchased from Sigma-Aldrich (Rehovot, Israel), and Boc-L-phenylalanine 4-nitrophenyl ester (L-pNPA), Boc-D-phenylalanine 4-nitrophenyl ester (D-pNPA) were obtained from Tzamal-D-Chem. All materials were used as received without further purification. Deionized (DI) water processed by a Millipore purification system (Darmstadt, Germany) with minimum resistivity of 18.2 MΩ cm were used for all the experiments.

UV-vis absorption spectroscopy

To determine the binding stoichiometry within the spontaneous F-Zn(II) crystallization process, UV-vis absorption titration experiments were performed by keeping the total concentration constant ([F] + [Zn(II)] = 2 mM) and changing the F and Zn(II) molar ratio. 2 mL sample solution was pipetted into a 1.0 cm path-length quartz cuvette, and the spectra were collected using a T60 visible spectrophotometer (PG Instruments, Leicestershire, United Kingdom) with a fixed 1 nm spectral bandwidth and a wavelength range of 200-800 nm. The aqueous NaOH solvent was used as background and subtracted. The ligand to metal charge transfer (LMCT) absorbance band at 380 nm was extracted to generate the Job Plot vs. mole fraction of Zn(II). Three measurements were performed and averaged for accuracy.

All catalysis reactions were recorded using Biotek Synergy HT plate reader (Biotek, Winooski, VT, USA) in 96-well UV-Star UV transparent plate (Greiner BioOne, Frickenhausen, Germany)

with normal reading speed and calibration before reading. The absorption spectra of DI water were recorded as background and subtracted. Three measurements were performed and averaged for accuracy.

Fourier transform infrared spectroscopy (FTIR)

The F-Zn(II) crystals were dispersed in anhydrous methanol and drop cast onto KBr IR card (International Crystal Labs, Garfield, New Jersey, USA) followed by vacuum drying at room temperature. The FTIR spectra were recorded on a Nicolet 6700 FTIR spectrometer (Thermo Scientific, Waltham, Massachusetts, USA), from 4000 to 400 cm^{-1} at room temperature. 128 scans were collected with a spectral resolution of 4 cm^{-1} in a nitrogen atmosphere. Background spectra (vacuum dried anhydrous MeOH on KBr) were recorded under identical conditions and subtracted.

Scanning electron microscopy (SEM)

A 10 µl aliquot of the solution of the structure was drop cast on a microscope glass coverslip dried at room temperature and sputtered with chromium. SEM images were taken using a JEOL JSM 6700F field emission scanning electron microscope (JEOL, Tokyo, Japan) operated at 10 kV.

Thermal gravimetric analysis (TGA)

TGA of the F and F-Zn(II) crystals was conducted using a TGA Q5000 V3.15 Build 263. The sample was heated under an air atmosphere at a heating rate of 10 °C/min.

Powder X-ray diffraction (XRD)

The normalized XRD patterns were obtained in symmetrical Bragg geometry with Cu Kα radiation on Scintag (USA) powder diffractometer equipped with liquid nitrogen-cooled Ge solid-state detector.

Computational details

All the monomer calculations were performed with density functional theory at the M06-2X/6-31+g(d,p) level of theory as implemented in the Gaussian 16 package. It is important to note that, in Gaussian 16,[1] the default grid is set to Ultrafine, and the accuracy of the two-electron integrals is kept at 10^{-12}. We did find that using these default settings is important to converge the calculations. For example, with the default settings of Gaussian 09 (fine grid and 10^{-10} accuracy for two-electron integrals), we generally encountered memory errors during the frequency and transition state calculations. All the thermochemistry calculations were performed at 300 K. Solvent effects were included both by considering 5 explicit water molecules in conjunction with the Polarizable Continuum Model (PCM). Frequency calculations were performed for all the optimized structures to understand the nature of the stationary state. We verified that all the transition states have a single imaginary frequency and all the other local minima have zero imaginary frequencies. In the energy diagram (Figure 4 of the main text), we have added the energy of an isolated pNPA to complexes **1**, **TS$_{1/2}$**, and **2** and we have added the energy of an isolated pNP to the complexes **6**, **TS$_{6/7}$**, and **7**. Optimized geometries of all the complexes are given in the **Supplementary Data 1**. For the dimer configuration, due to the larger system sizes, all the calculations were performed at M062X/6-31g(d) level of theory. However, as explained in the next sections, some of the results were also verified at M062X/6-31+g(d,p) level of theory.

Supplementary Table 1. Crystallographic Data collection and refinement statistics

|	F-Zn(II)
Data collection	
Space group	$P2_1$
Cell dimensions	
a, b, c (Å)	5.57, 31.54, 9.50
α, β, γ (°)	90.0, 90.0, 90.0
Resolution (Å)	0.90 (0.92-0.90)[a]
R_{merge}	0.058 (0.065)
$I/\sigma(I)$	21.6 (15.6)
$CC_{1/2}$	99.7 (99.4)
Completeness (%)	91.3 (82.4)
Redundancy	5.2 (3.6)
Refinement	
Resolution (Å)	0.90
No. reflections	2231
R_{work} / R_{free}	0.038 / 0.039
No. atoms	
Protein	88
Zinc ion	2
Water	0
B factors (Å^2)	
Protein	2.9
Ligand/ion	2.0
R.m.s. deviations	
Bond lengths (Å)	0.016
Bond angles (°)	1.8

[a]Values in parentheses are for the highest-resolution shell.
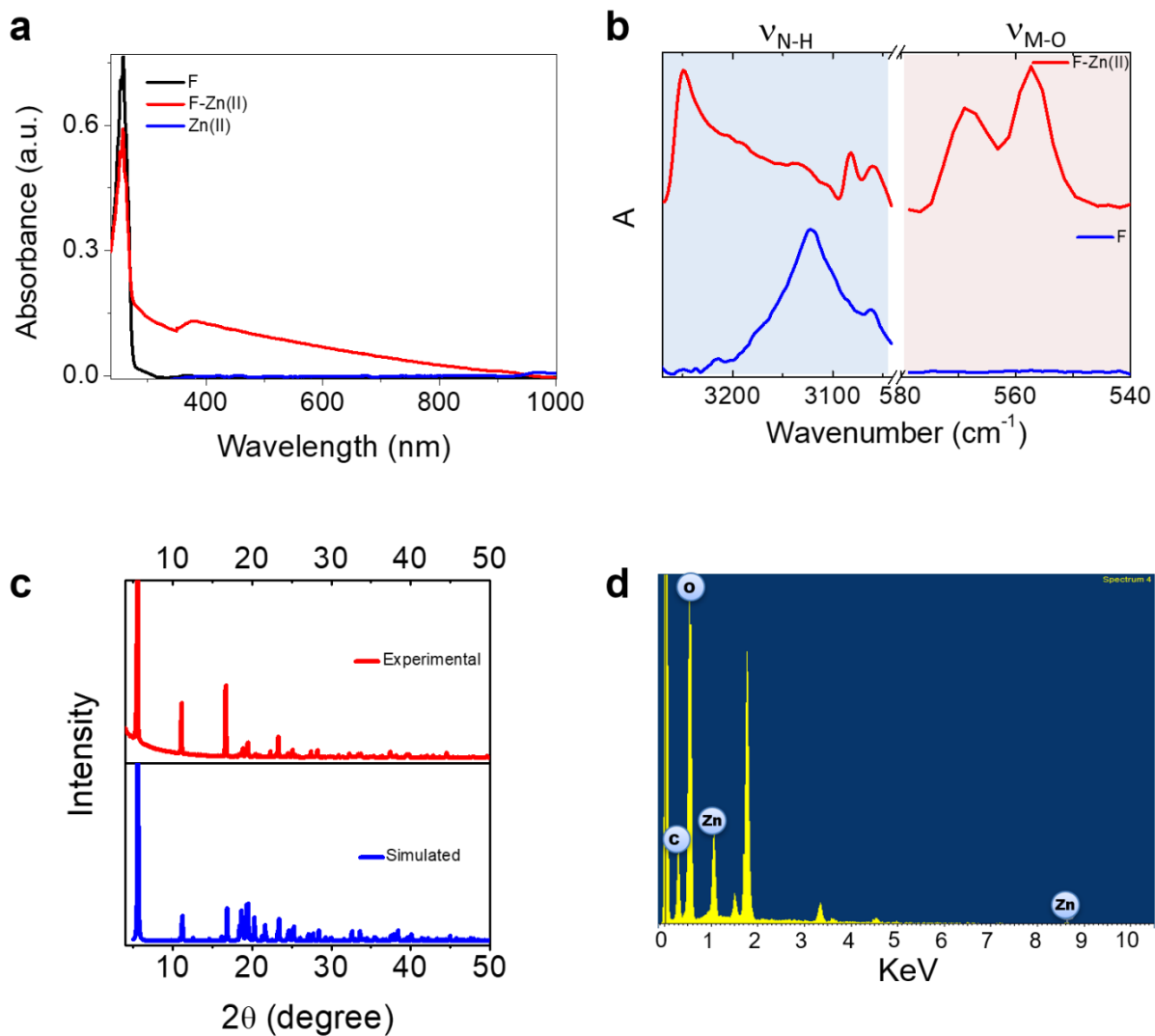
Supplementary Figure 1. Spectroscopic characterization of F-Zn(II). a, UV-vis absorption spectra. **b**, FTIR spectra (3270–3040 (ν_{N-H}) and 580–540 cm^{-1} (ν_{M-O}) region) of phenylalanine (F) and F-Zn(II). **c**, Powder X-ray diffraction patterns. **d**, EDS spectra.
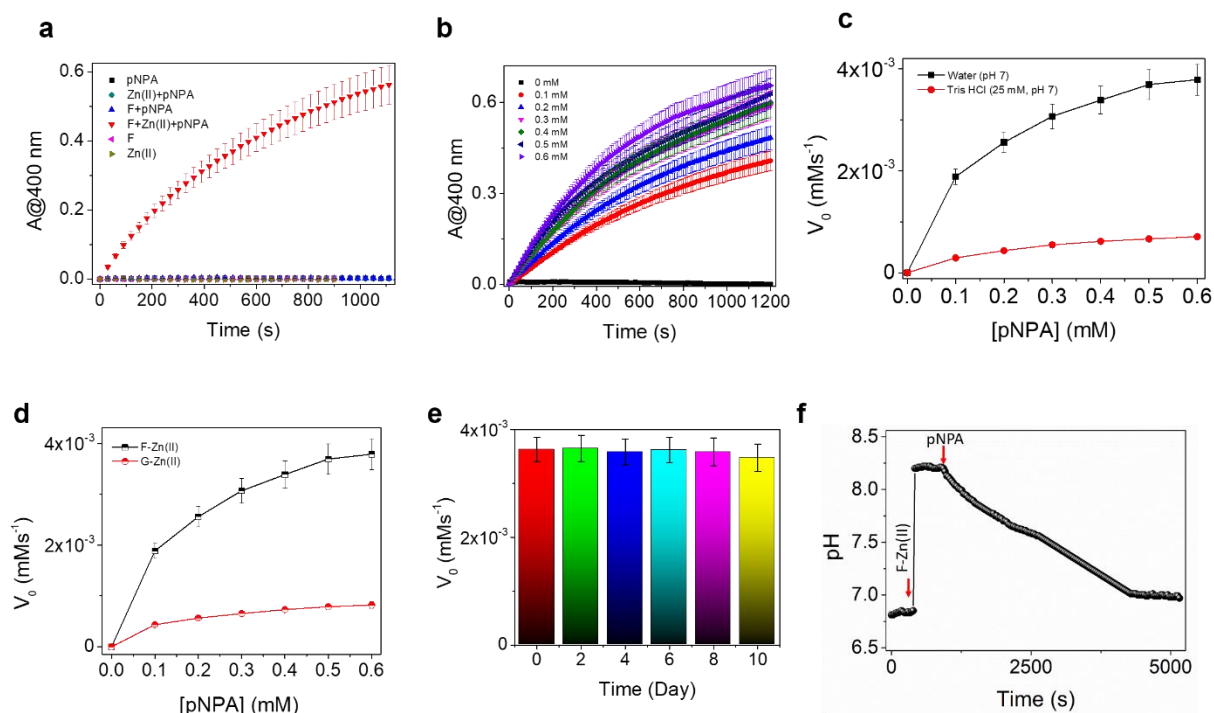
Supplementary Figure 2. Esterase activity of F-Zn(II), a, Esterase activity experiments show that the F-Zn(II) crystals are capable of hydrolyzing pNPA into coloured product NP monitored at λ_{max} = 400 nm. No hydrolysis was taken place when phenylalanine (F) or Zn(II) omitted from the system. **b**, The plot of absorbance (A at 400 nm) versus time at different concentrations of substrate (pNPA) in the presence of F-Zn(II) catalyst. **c**, The comparison of Initial rate (V_0) of pNPA hydrolysis catalyzed by F-Zn(II) as a function of substrate concentration in DI. water (pH 7) and Tris-Hcl (25 mM, pH 7) buffer. **d**, The comparison of Initial rate (V_0) of pNPA hydrolysis catalyzed by F-Zn(II) and G-Zn(II) as a function of substrate concentration. **e**, Time-dependent Initial rate (V_0) of pNPA hydrolysis catalyzed by F-Zn(II) in DI. Water, a negligible change in the catalytic rate of the reaction ruling out any influence of dissolved impurities and pH changes over time. Error bars in all graphs represent standard deviations of at least three independent measurements. **f**, Time-dependent in situ pH changes during the catalytic reaction process (red arrows indicating the addition of F-Zn(II) catalyst (at T= 390 s) and pNPA substrate (at T= 900 s) in DI. water.
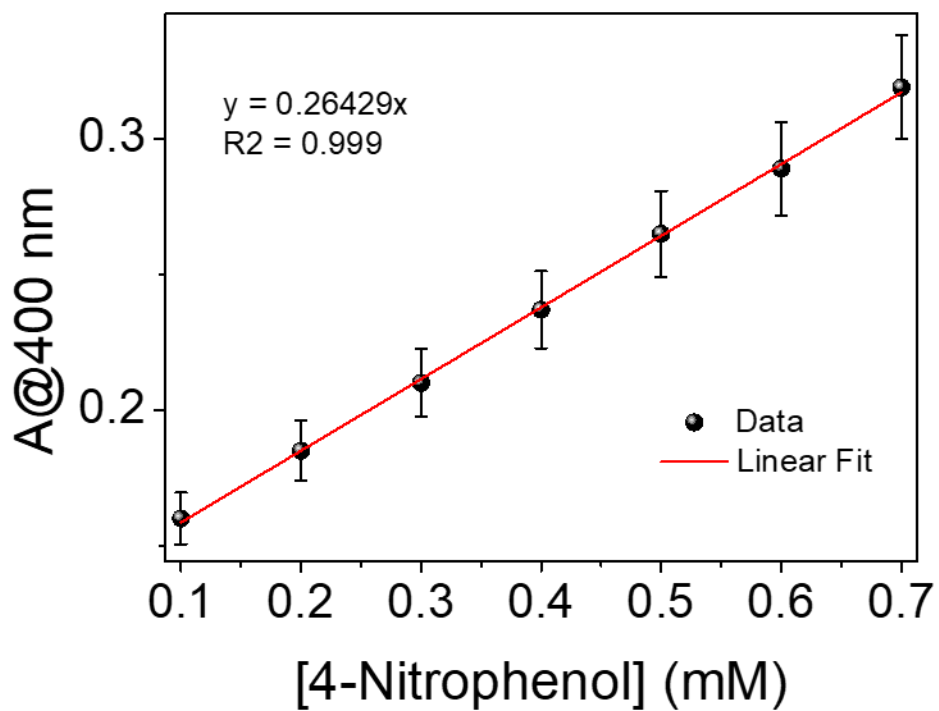
Supplementary Figure 3. The product calibration curve, the absorbance (A) at 400 nm of 4-nitrophenol standard solution at various concentrations, the slope of the linear fit determines the extinction coefficient. Error bars represent standard deviations of at least three independent measurements.
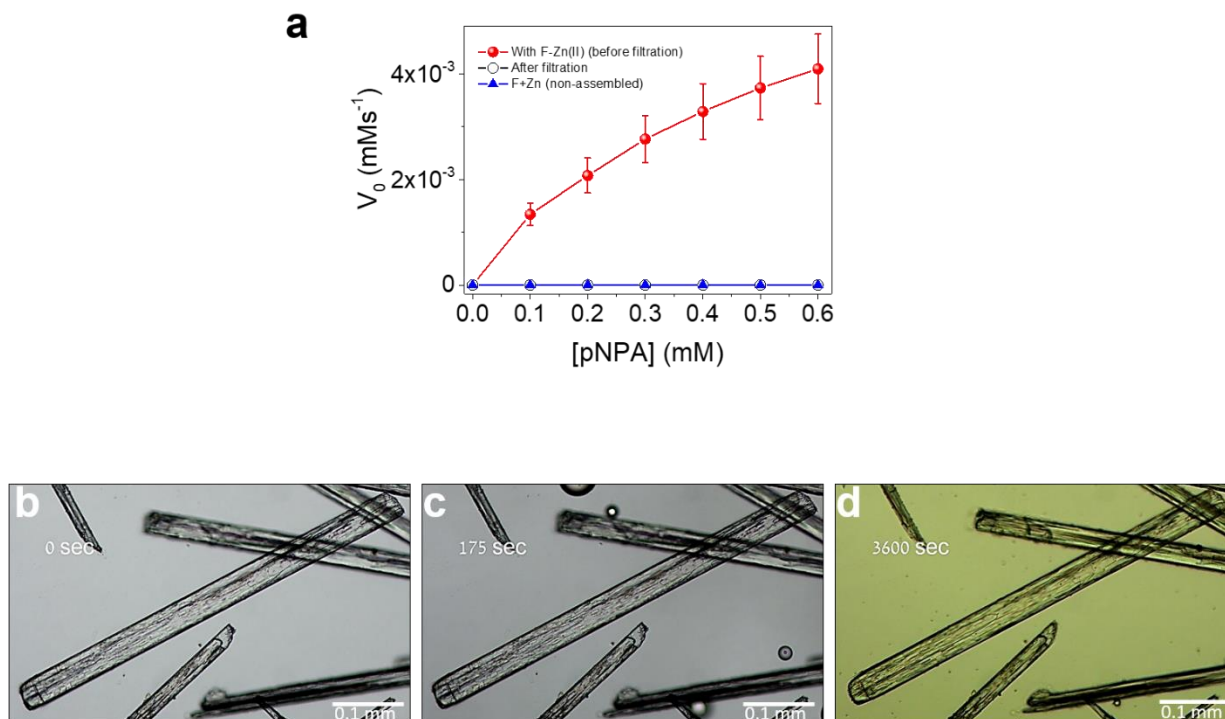
Supplementary Figure 4. F-Zn(II) single crystals are responsible for catalysis. **a**, Catalytic activity before and after filtrate passing an aqueous suspension F-Zn(II) through a 100 nm filter shows that the active species are unable to permeate the filter. Error bars represent standard deviations of at least three independent measurements. b, c and d Optical microscopy snapshots are taken from Supplementary Video 3, in-situ monitoring the F-Zn(II) catalytic hydrolysis of pNPA in DD water captured every 5s. b) F-Zn(II) crystals, c) and d) F-Zn(II) crystals just after the addition of substrate pNPA and after 57 min respectively, the colour change in the reaction solution suggesting the formation of hydrolyzed product PNP.
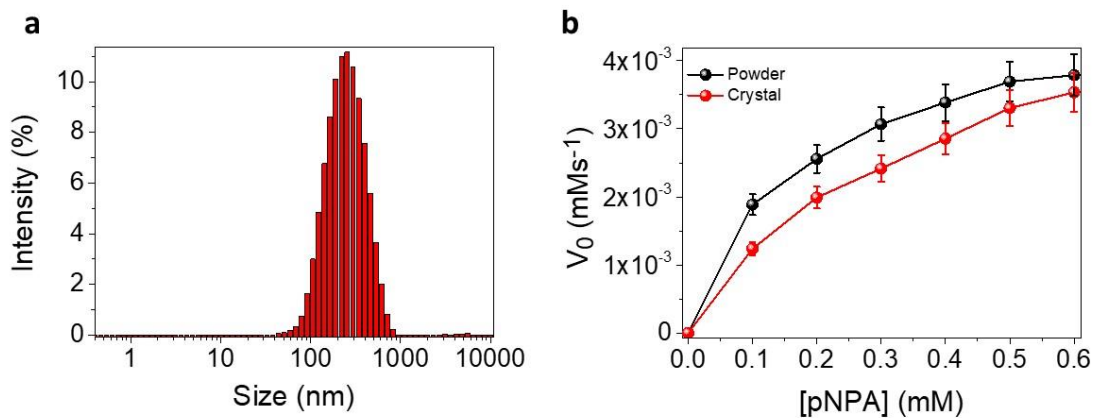
**Supplementary Figure 5. The influence of F-Zn(II) size on pNPA hydrolysis**. a) Dynamic light scattering (DLS) spectra of ground F-Zn (II) dispersion in DI water. b) Initial rate (V_0) of hydrolysis catalyzed by ground powder and crystals of F-Zn (II) as a function of substrate concentration, with the smooth Michaelis–Menten curve fitting. Error bars represent standard deviations of at least three independent measurements.
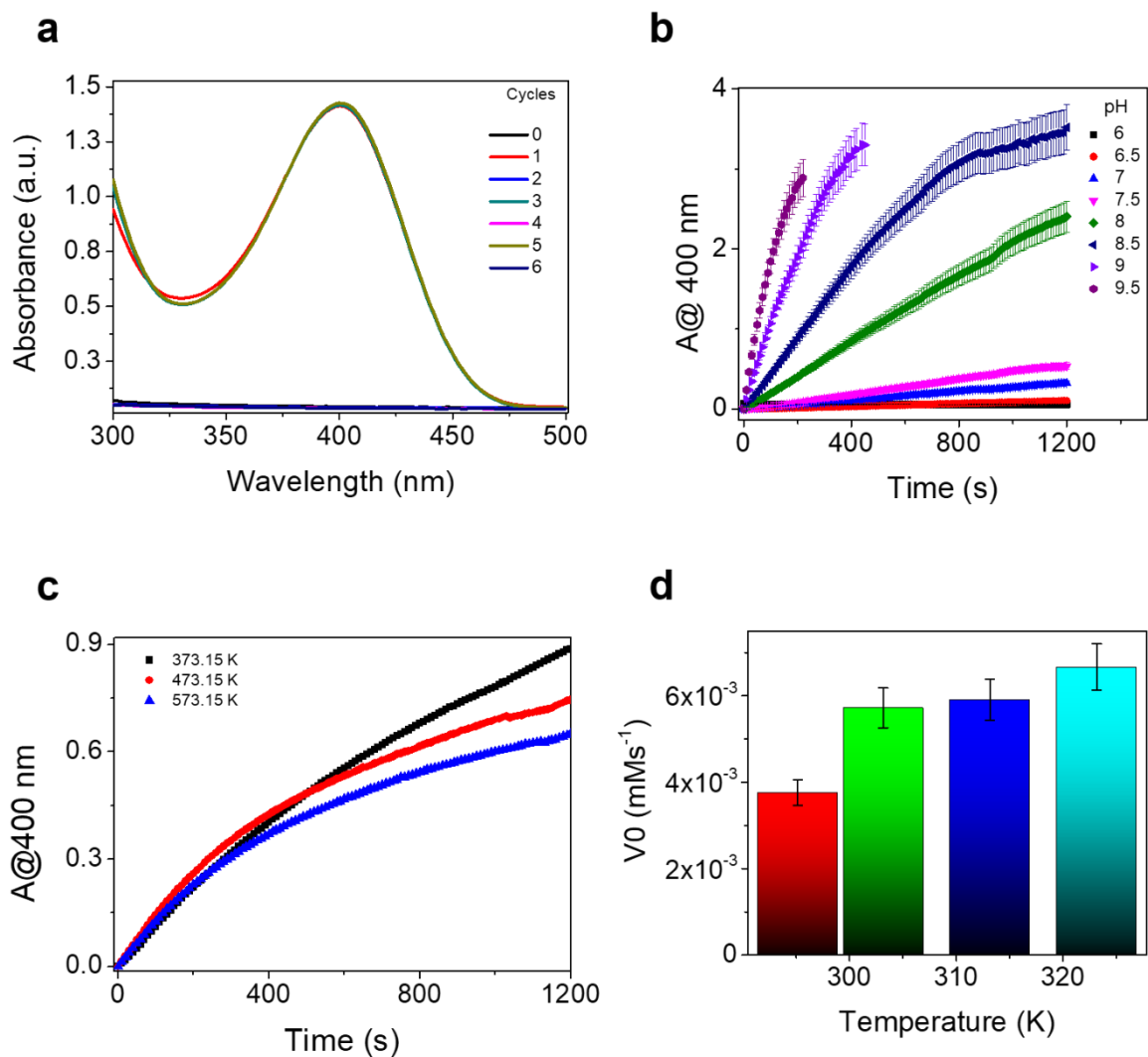
Supplementary Figure 6. F-Zn(II) esterase catalytic stability experiments, a, catalyst reusability experiment showing UV-vis absorption spectra after cycle of the addition of substrate (pNPA, 1, 3, and 5) and washing (0, 2, 4 and 6). **b**, pH-dependent esterase activity performed in Tris-HCl (25mM) buffer solution. **c**, the thermal catalytic stability of F-Zn(II). the catalyst was annealed at different higher temperatures (373.15 K, 473.15 K and 573.15 K) and compared its esterase activity measured at room temperature. d, F-Zn(II) catalytic pNPA hydrolysis rate at different reaction temperatures. Error bars in all graphs represent standard deviations of at least three independent measurements.
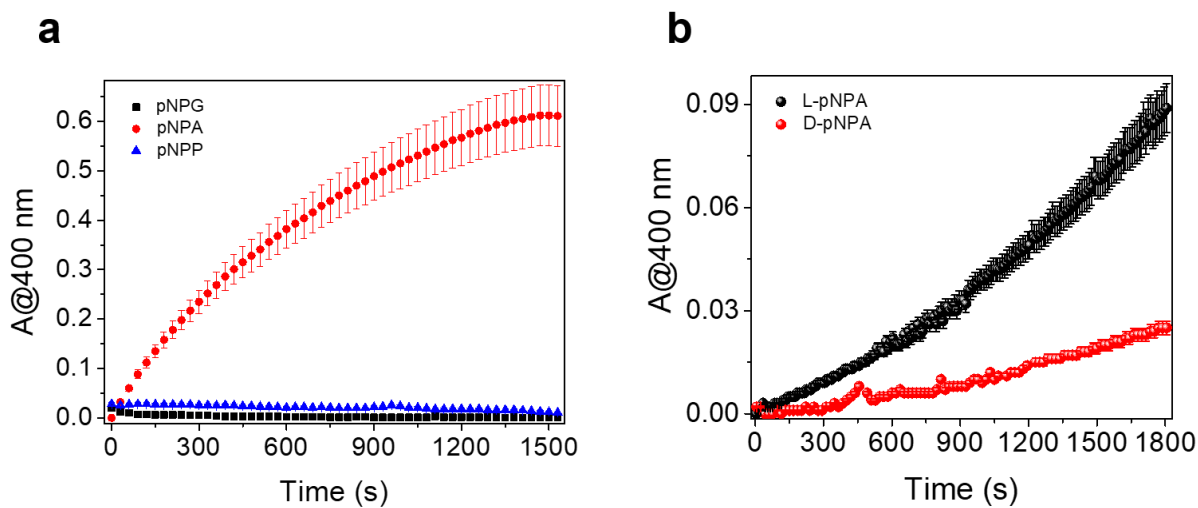
Supplementary Figure 7. Substrate specificity experiments, a, F-Zn(II) esterase activity in the presence of chemically distinct substrates (pNPG, pNPA and pNPP). **b**, F-Zn(II) esterase activity in the presence of two enantiomeric substrates (L-pNPA and D-pNPA). Error bars in all graphs represent standard deviations of at least three independent measurements.
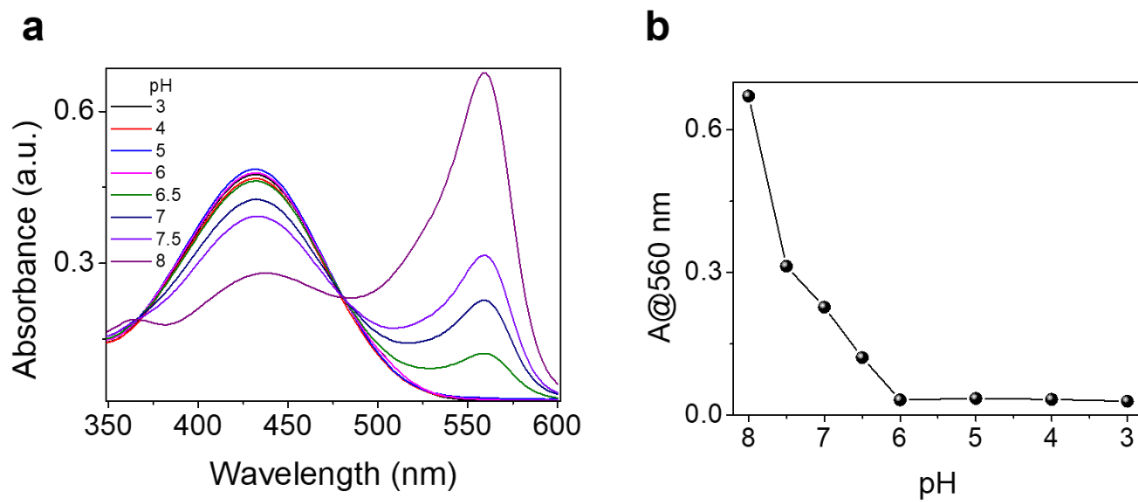
Supplementary Figure 8. Phenol red pH calibration curve. a, pH-dependent UV-vis absorbance spectra of phenol red (50 μM) in Tris buffer (20 mM) solution. **b**, The change in absorbance at 560 nm as a function of pH.
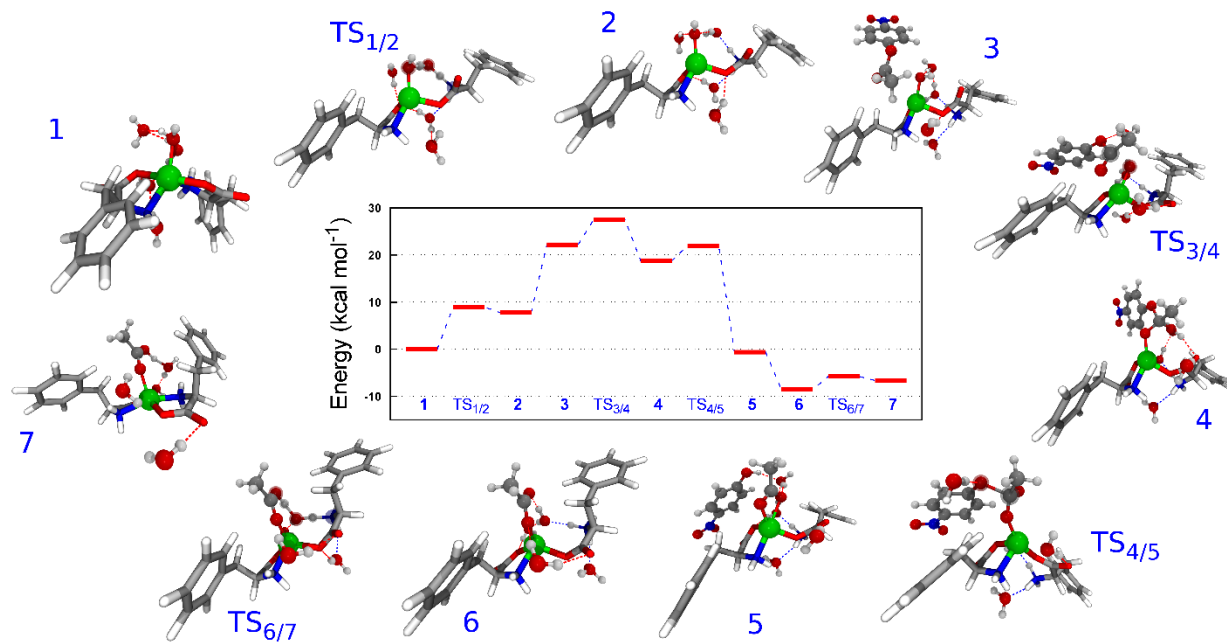
Supplementary Figure 9: F-Zn(II) catalytic esterase reaction mechanism and the optimized structures along the reaction pathway. The monomer F-Zn(II) catalytic complex is represented in stick mode; and waters and pNPA are shown in CPK mode. Atoms involved in the transition are also highlighted in their respective transition state structures. The calculated free energy profile is shown at the centre.

Supplementary Discussion

Effect of aggregation on the reaction mechanism

Based on our calculations with the monomer and also from our experiments, we are quite sure that the pNPA hydrolysis occurs only at the Zn-sites and we strongly believe that this will be the case even when the reaction occurs on a crystal surface. As such, we do not expect any major changes in the reaction mechanism that we have presented in the main text. However, we do anticipate some differences in the reaction mechanism between a monomer and a crystal that could reduce the overall energy difference between step-1 and $TS_{3/4}$ (which is an important factor in deciding

the feasibility of pNPA hydrolysis at the Zn site). Two of the main differences that we anticipate include: (i) the transfer site of the proton and (ii) the approach of the pNPA molecule towards the hydroxide ion (of the water) bound to the Zn-site (hereafter, referred to as the active Zn-site). Through our calculations described below, we explain how each of these changes affects the overall reaction barrier (the free energy difference between step-1 and $TS_{3/4}$).

**i) Effect of proton-transfer site on the energy barrier**

To explore the effect of the proton-transfer site on the energy barrier, we have considered three sites for the proton transfer. As shown in Supplementary Figure 10, we transferred the proton from the Zn-bound H_2O molecule to either the COO (Supplementary Figure 10a) or to one of the two NH_2 groups (Supplementary Figure 10a and c) attached to the active Zn-site and compared their energy with respect to step-1 (the transfer of a proton from the water to any of these groups corresponds to step-2). Among these three configurations, we find that the configuration corresponding to the transfer of a proton to the COO group (Supplementary Figure 10a) is the most favourable one. Also, this configuration brings minimal changes to the geometry of the dimer and we expect a similar behaviour also in the crystal. On the other hand, the proton transfer to the NH_2 group shown in Supplementary Figure 10b (hereafter, referred to as the densely packed side – On the (100) surface, this side has a dense packing of PA rings) results in a large change to the dimer structure. Although this structure (Supplementary Figure 10b) possess a reasonable energy (~ 6 kcal/mol above step-1) when compared to the monomer's step-2 energy (7.77 kcal/mol above monomer's step-1), we anticipate that this structure would be less feasible in the crystal configuration as it requires the breaking of aromatic stacking (the phenyl-phenyl stacking). Finally, the transfer of a proton to the NH_2 group as shown in Supplementary Figure 10c (hereafter, referred

to as sparsely packed side) brings reasonable changes to the dimer structure but it is energetically

less stable (15 kcal/mol above step-1).

Supplementary Figure 10: Step-2, proton transfer to the (a) COO group, (b) NH_2 group on the dense packing side (towards the reader's view), and (c) NH_2 group on the sparse packing side (away from the reader's view). The proton transfer sites were marked with circles.
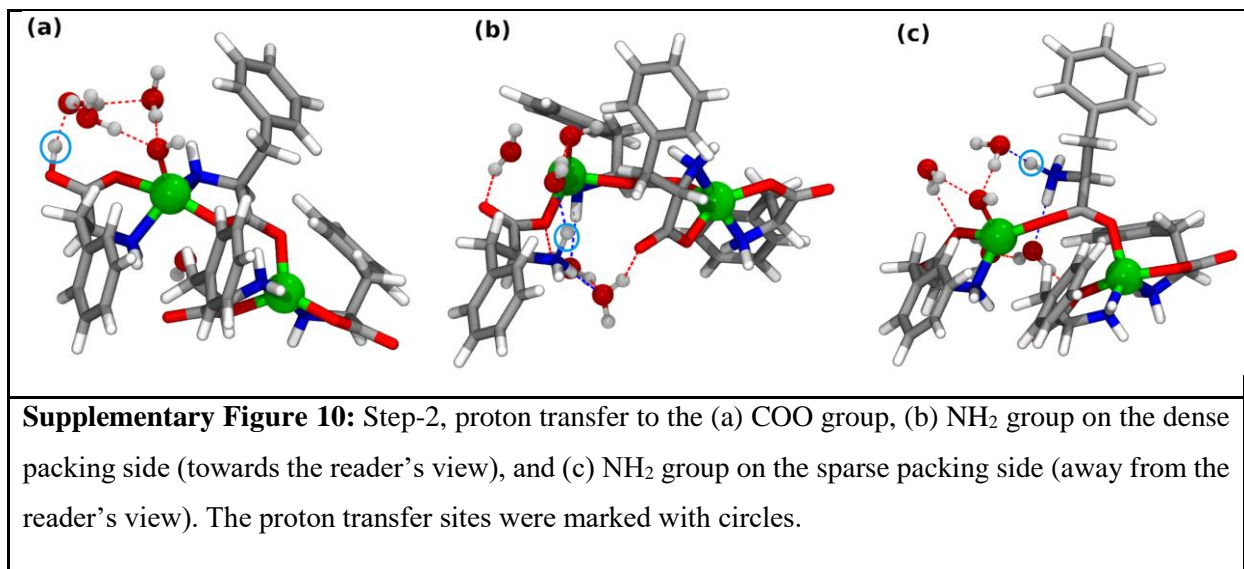
Thus, although our monomer and dimer results suggest that a proton transfer to one of the

NH_2 groups is energetically feasible, considering the structural and energetic changes that we

observed with such a transfer in the dimer configuration, we conjecture that a proton-transfer to

the COO group would be the most probable scenario in the crystal structure. Our conjecture is

based on our new computational results on the dimer configuration that clearly show (i) a lower

energy difference between step-1 and step-2 (see Table S2), (ii) a lower $TS_{1/2}$ barrier (see Table

S2) and (iii) minimal changes to the aggregate structure when we transfer a proton to the COO

group of the active site (compare Supplementary Figure 10a-c). Also, as noted in the main text,

for the case of the monomer the transfer of a proton to (from) any NH_2 group requires it to move

away from (closer to) the active Zn-site and in the crystal, this corresponds to a change in the

stacking configuration. The transfer of a proton to the COO group does not require such changes, further supporting our conjecture.
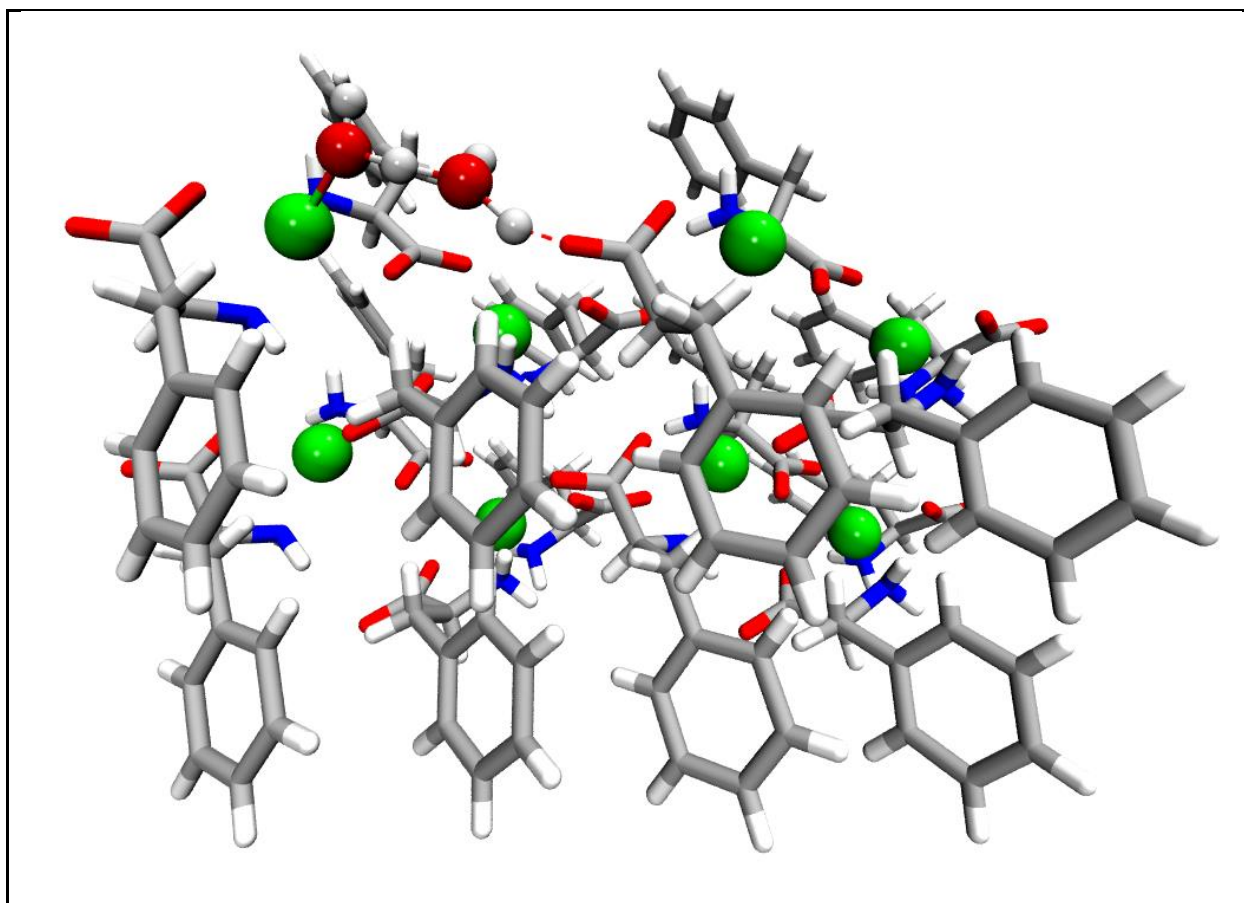

Supplementary Figure 11: $TS_{1/2}$, proton transfer to the COO group bound to the active site.
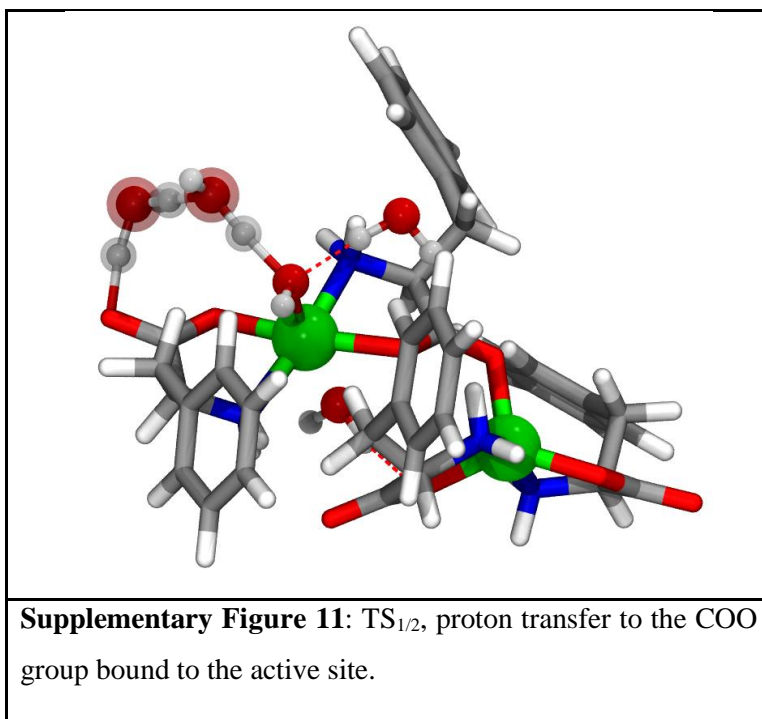
Supplementary Table 2: Energy of Step-2 calculated for various sites of proton transfer in the dimer model

Proton transfer site	Energy with respect to the dimer's Step-1 energy (kcal/mol)
COO group	1.2
NH_2 group away from us in Figure A1	15.8
NH_2 group towards us in Figure A1	6.04

Supplementary Table 3: Comparison of the energy barrier for the proton transfer ($TS_{1/2}$) in monomer and dimer models

Proton transfer site	Energy of the $TS_{1/2}$ with respect to the Step-1 (kcal/mol)
Monomer	6.1
Dimer	8.9

It is worthwhile to mention that, in a crystal, there are several other possibilities available for the proton transfer. Some of these possibilities include the transfer of the proton from the active Zn-site to the NH_2 or COO groups bound to the nearest-neighbour Zn-site or to the COO groups bound to the next-nearest-neighbour Zn-site through the formation of a proton bridge (formed by other water molecules available as the solvent). Among these possibilities, we find that the transfer of a proton to the COO group of the next-nearest-neighbour Zn-site to be an interesting one. As shown in Supplementary Figure 12, it might be possible to transfer the proton to this COO group with just a single water molecule acting as a bridge. Also, as can be easily noticed, this COO group is equivalent to the COO group of Supplementary Figure 10a (except that it is bound to the next-nearest-neighbour Zn-site instead of the active Zn-site). As we could only stabilize the $TS_{1/2}$ of the Supplementary Figure 10a configuration with two water molecules (see Supplementary Figure 11) and as forming a proton-transfer-bridge with a single water molecule would be more favourable than forming a proton-transfer-bridge with two water molecules, we believe that the configuration in Supplementary Figure 12 would be the most favourable configuration for the proton transfer in a crystal. However, we could not prove this statement due to the need to consider, at least, a tetramer in our calculations to explore this configuration.
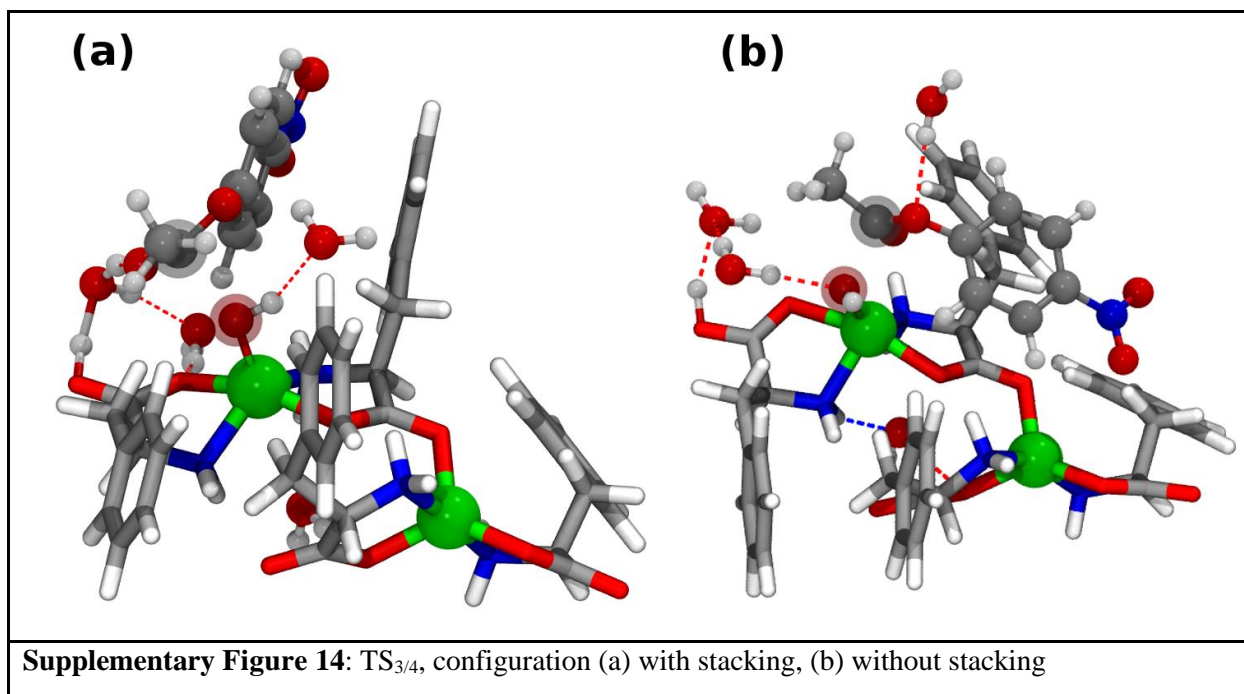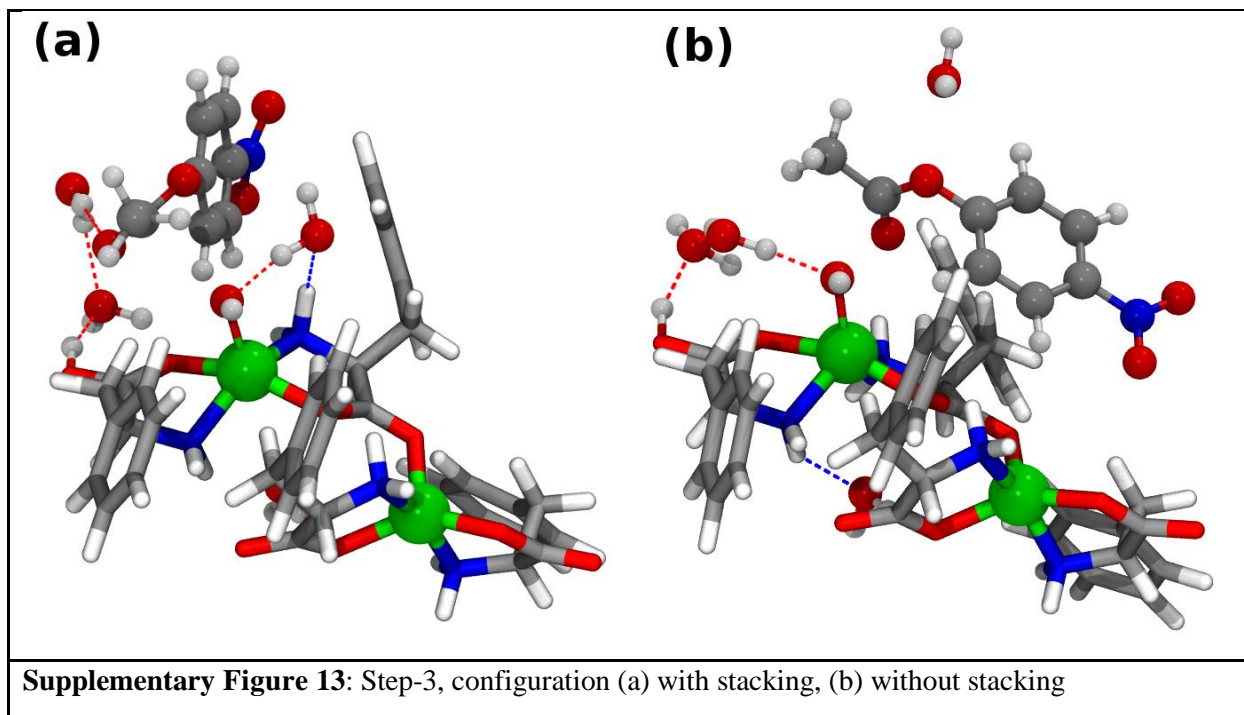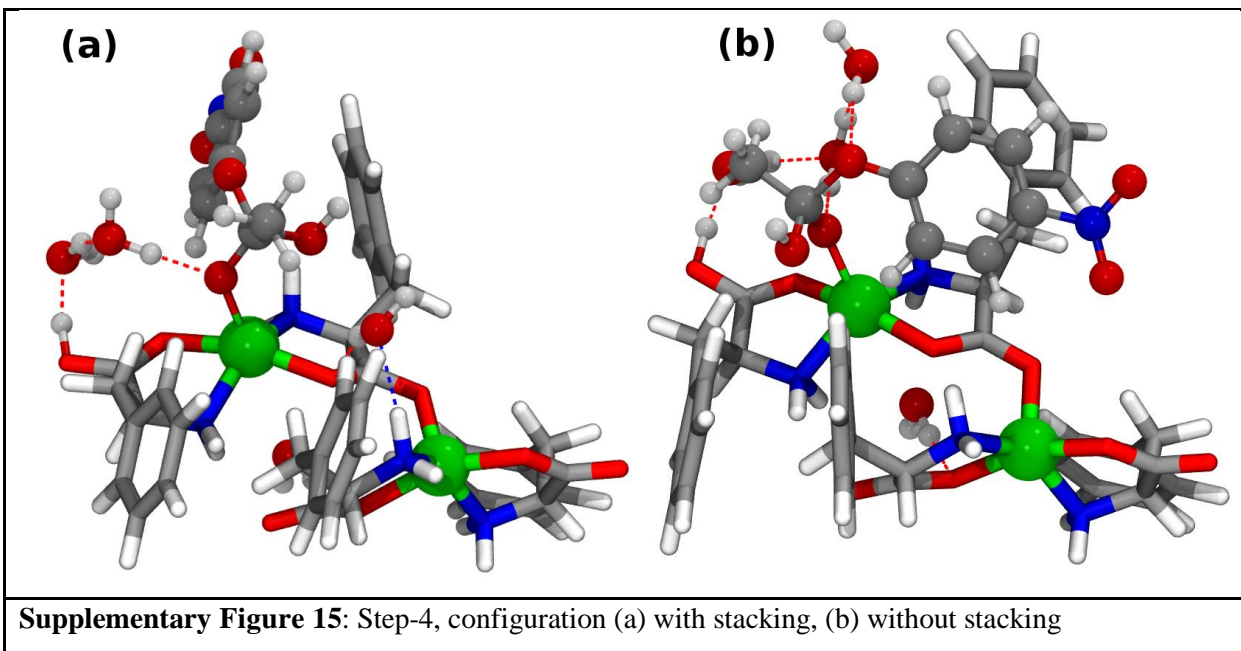
Supplementary Figure 12: Proton transfer from the water bound to the active Zn-site to the COO group of the next-nearest-neighbour Zn-site on the (100) surface. This is one of the configurations where the proton transfer does not require a change in the crystal structure and just involves a single water molecule acting as a bridge between the proton donor and acceptor sites. In the crystal, we believe that this configuration would be the most probable one for the proton transfer.

ii) Effect of the pNPA molecule's approach on the energy barrier

In this section, we have considered two different paths for the pNPA molecule to approach the Zn-bound hydroxide ion, and both of these configurations are shown in Supplementary Figure 13. Between the two configurations, we find the configuration in which the pNPA molecule approaches the active Zn-site from the sparsely-packed side (see Supplementary Figure 13a) of the crystal to be the most stable configuration. On the (100) surface of the crystal, the sparsely-

packed side corresponds to the approach of a pNPA molecule from the rear side of the Supplementary Figure 12 (away from the reader's viewpoint). The enhanced stability for the configuration in Supplementary Figure 13a is mainly due to the presence of additional aromatic stacking interactions between the phenyl rings of pNPA and the phenylalanine. Due to the lack of such additional stacking for the configuration in Supplementary Figure 13b, it is found to be energetically less stable compared to the configuration depicted in Supplementary Figure 13a. Furthermore, due to the asymmetry in the stacking, the approach of a pNPA molecule from the densely-packed side (closer to the reader's viewpoint in Supplementary Figure 12) will be less probable, and our attempts to consider this approach led to large changes in the crystal packing. For step-3 (pNPA molecule approaching the active Zn-site), the stacked configuration is found to be ~ 5 kcal/mol more stabilized compared to the unstacked configuration. This difference in the energies between stacked and unstacked configurations is also present in steps $TS_{3/4}$ and step-4 (see Supplementary Figure 14 and 15 for the respective structures), where the stacked configuration is more stable by ~ 7.8 kcal/mol and 4 kcal/mol, respectively.

Supplementary Figure 13: Step-3, configuration (a) with stacking, (b) without stacking

Supplementary Figure 14: TS$_{3/4}$, configuration (a) with stacking, (b) without stacking

S21

Supplementary Figure 15: Step-4, configuration (a) with stacking, (b) without stacking

### iii) Energy differences between the monomer and the dimer

Based on the results from the above two sections, we find that stacking alone can play a large role in reducing the energy barrier for the pNPA hydrolysis at the active Zn-site. Indeed, we find that the $TS_{3/4}$ energy barrier in the monomer (26.7 kcal/mol) and the unstacked configurations (27.5 kcal/mol) are very close to each other. Furthermore, the difference in the energy barrier (between step-1 and $TS_{3/4}$) between the monomer and the stacked configuration of the dimer is ~ **8.5** kcal/mol (note that the energy barrier difference between the stacked and unstacked configurations in the dimer model is ~ 7.8 kcal/mol). Both of the above energy differences emphasize the role of stacking in this hydrolysis reaction. Apart from the above, as we move from the monomer to the dimer, the reaction between steps 3 and 4 was found to be more exothermic (by 8.2 kcal/mol). This increase in the release of energy is expected to promote the next steps of the reaction. *Finally, we*

foresee that all of the above effects (decreased barrier for proton transfer with minimal structural changes, decreased barrier for the approach of a pNPA molecule towards the active Zn-site due to the additional aromatic stacking interactions, and increased exothermicity between the steps 3 and 4) will be further enhanced in the crystal structure and will facilitate the pNPA hydrolysis at the active Zn-site.

Finally, to verify the robustness of the above predictions, we have also calculated the energies of steps 1, 2, and 3 at the M062X/6-31+g(d,p) level of theory and we find that these energy values are within 2 kcal/mol of the values obtained at the M062X/6-31g(d) level of theory indicating the accuracy of our results. We would also like to note that, although we were able to optimize the step4 with the 6-31+g(d,p) basis, we ran into memory issues while calculating the frequencies (which are required to calculate the thermochemical data). Furthermore, all our attempts to stabilize the transition states were unsuccessful (we were unable to proceed even when we read the 6-31g(d) frequencies as a guess for the 6-31+g(d,p) calculation. In the case of the monomer, this approach of reading the frequencies from a lower-level theory calculation to predict the transition states with 6-31+g(d,p) basis was fruitful).

Supplementary Figure 16: Free energy differences among steps 1 to 4 in the monomer and the dimer.
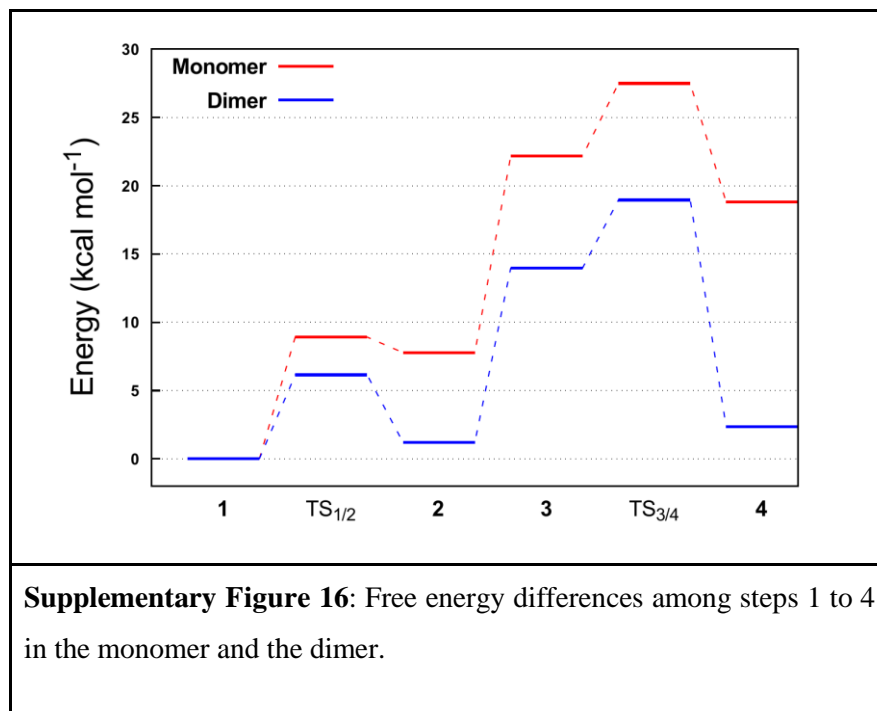
The calculated free energies of the steps 1, $TS_{1/2}$, 2, 3, 4, and $TS_{3/4}$ at the M062X/6-31g(d) level of theory for the configurations corresponding to a proton transfer to the COO group and the pNPA molecule approaching the Zn-site by forming a stacked configuration are given in Supplementary Figure 16. In the same figure, we have also presented the monomer results for these steps for a comparison.
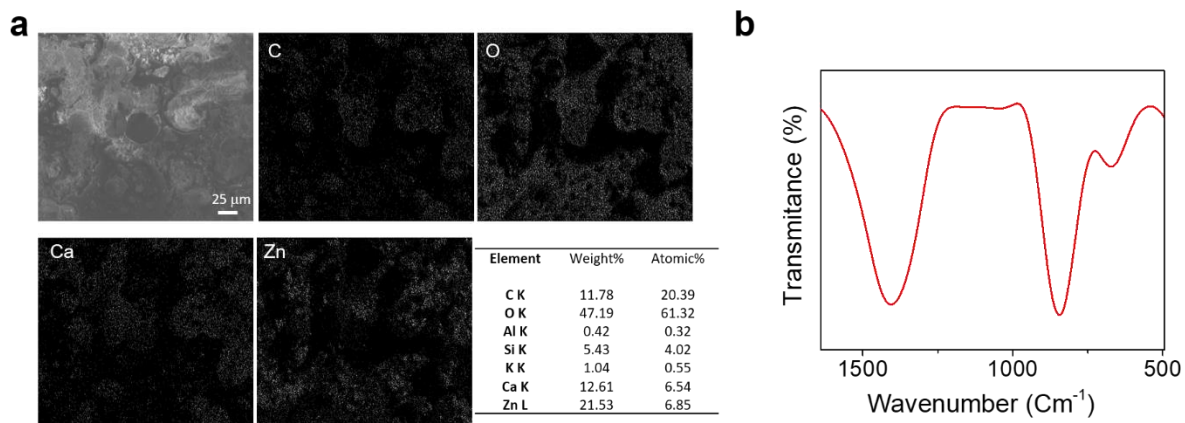
Supplementary Figure 17. CO₂ sequestrated CaCO₃ characterization. a, EDS colour mapping for C, O, Ca, Zn and EDS analysis table. **b**, FTIR spectra.

Supplementary References

1. Frisch, M. J. et al. Gaussian 16, Revision B.01. *Gaussian Inc., Wallingford CT* (2016)